2-12-2008

A Coupled Electrochemical and Hydrodynamical Two-Phase Model for the Electrolytic Pickling of Steel

Nulifer Ipek
University of Pennsylvania

Michael Vynnycky
University of Pennsylvania

A. Cornell
Royal Institute of Technology

Suggested Citation:
A. Ipek, M. Vynnycky, and A. Cornell. (2008). "A Coupled Electrochemical and Hydrodynamical Two-Phase Model for the Electrolytic Pickling of Steel." *Journal of the Electrochemical Society.* **155** (4). P33-P43.

A Coupled Electrochemical and Hydrodynamical Two-Phase Model for the Electrolytic Pickling of Steel

Abstract
In industrial electrolytic pickling, a steel strip with oxidized surfaces is passed through an aqueous electrolyte between a configuration of electrodes, across which a potential difference is applied. The strip is thereby indirectly polarized, and electrochemical reactions at the strip surface result in the dissolution of the oxide layer and the evolution of hydrogen and oxygen bubbles. In this paper, we extend an earlier mathematical model for the electrochemical aspects of the process, which took account only of the liquid phase, to include the effect of the gas phase. The model is two-dimensional, steady-state and isothermal, and comprises five ionic species, the mixture velocity, pressure, and the gas fraction; numerical solutions of this model are then obtained. The results of the single and two-phase models are compared, and their implications for the actual pickling process are discussed

Disciplines
Engineering | Mechanical Engineering

Comments
Suggested Citation:
A. Ipek, M. Vynnycky, and A. Cornell. (2008). "A Coupled Electrochemical and Hydrodynamical Two-Phase Model for the Electrolytic Pickling of Steel." *Journal of the Electrochemical Society.* **155** (4). P33-P43.

Journal of The Electrochemical Society, **155** (4) P33-P43 (2008)
0013-4651/2008/155(4)/P33/11/$23.00 © The Electrochemical Society

A Coupled Electrochemical and Hydrodynamical Two-Phase Model for the Electrolytic Pickling of Steel

N. Ipek,[a,d] M. Vynnycky,[b,e,z] and A. Cornell[c]

[a]*Department of Mechanical Engineering and Applied Mechanics, University of Pennsylvania, Philadelphia, Pennsylvania 19104, USA*
[b]*Department of Mechanics, and* [c]*Department of Chemical Engineering and Technology, Applied Electrochemistry, Royal Institute of Technology, SE-100 44 Stockholm, Sweden*

In industrial electrolytic pickling, a steel strip with oxidized surfaces is passed through an aqueous electrolyte between a configuration of electrodes, across which a potential difference is applied. The strip is thereby indirectly polarized, and electrochemical reactions at the strip surface result in the dissolution of the oxide layer and the evolution of hydrogen and oxygen bubbles. In this paper, we extend an earlier mathematical model for the electrochemical aspects of the process, which took account only of the liquid phase, to include the effect of the gas phase. The model is two-dimensional, steady-state and isothermal, and comprises five ionic species, the mixture velocity, pressure, and the gas fraction; numerical solutions of this model are then obtained. The results of the single and two-phase models are compared, and their implications for the actual pickling process are discussed.
 [DOI: 10.1149/1.2835224]

Manuscript submitted September 3, 2007; revised manuscript received December 13, 2007.
Available electronically February 12, 2008.

Electrochemical neutral pickling is a process that is widely used in industry to remove surface oxide layers formed during the continuous casting, reheating, hot-rolling, and annealing phases of the steelmaking process. The oxide layers are generally thought to consist of Cr_2O_3, Fe_2O_3, and $(Fe,Cr)_3O_4$ spinel, as well as possibly FeO, $NiFe_2O_4$, Fe_3O_4, and $(Fe,Cr)_2O_3$.[1] These are removed by means of a combination of conventional mixed acid and electrochemical neutral pickling; however, because the latter is considerably more environmentally friendly, it is of importance to optimize it to enable reduced use of the former.

The most common type of electrochemical pickling process consists of an electrically neutral bath containing sodium sulfate solution in turbulent flow at temperatures between 65 and 85°C. Pairs of anodic and cathodic electrodes are used to form half-cells that face the upper and lower surfaces of a moving steel strip, which passes horizontally in the gap between the electrodes. Polarization of the strip is achieved without contact and the anodic current density ranges between 0.5 and 3 kA m^{-2}.[2] Recent years have also seen increased interest in vertical-mode pickling,[3-5] for which the current density at the steel-strip surface has been reported to be as high as 5.5 kA m^{-2}.[5] A schematic of this process is given in Fig. 1, which shows a vertical pickling tank, along with the arrangement of anode and cathode electrodes and a steel strip which moves between the electrodes. Further information on many aspects of the pickling of austenitic stainless steels can be found in a recent survey by Li and Celis.[1]

Most existing theoretical work on electrochemical neutral pickling focuses on determining reaction mechanisms[6-11] rather than on the industrial process or geometric configuration. The only earlier attempts to model the pickling process as a whole, i.e., the half-cell, rather than focusing solely on the electrochemical details of the anodic cycle, have been due to Ipek et al.[12-14] In Ref. 12, the steel strip was assumed to be stationary and ionic transport due to convection and diffusion, as well as the gas phase, was neglected. Ipek et al.[13] considered, in a simplified way, the reactions for the evolution of hydrogen gas at the cathode and cathodic sections of the steel strip and oxygen gas at the anode and anodic sections of the steel strip; it is the latter reaction that occurs simultaneously with the removal of the surface oxide layers. In particular, as a first step toward understanding the effect of gas evolution on the process, Ipek et al.[13] computed the secondary current distribution and calculated an averaged global value for the gas fraction. The work in Ipek et al.[14] was an extension of that in Ref. 12, in that the steel strip was assumed to translate with a uniform speed, and ionic transport due to convection, diffusion, and migration was included, although the presence of the gas phase was neglected.

In this paper, we extend the work in Ref. 14 by adding a more detailed hydrodynamical model, which includes not only the role of electrolyte convection but also hydrogen and oxygen bubble evolution. As in our earlier work,[14] we consider vertical-mode pickling, which is known commercially as the Neograv process;[5,15] from the theoretical point of view, one motivation for considering this, ahead of horizontal-mode pickling, is that there already exists some literature for bubbly two-phase flow adjacent to vertical electrodes in binary solutions,[16-20] although the electrochemical aspects in such

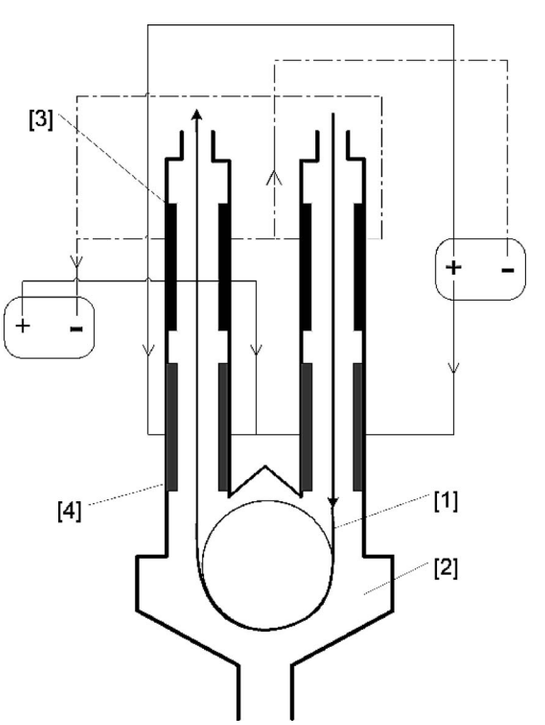

Figure 1. Schematic illustration of a vertical electrolytic pickling tank: [1] the steel strip, [2] the electrolyte, [3] the cathode, and [4] the anode, situated on both sides of the vertical steel strip.

[d] Present address: Västra Bangatan 33D, 195 40 Märsta, Sweden.
[e] Present address: Department of Mathematics and Statistics, University of Limerick, Limerick, Ireland.
[z] E-mail: michael.vynnycky@ul.ie

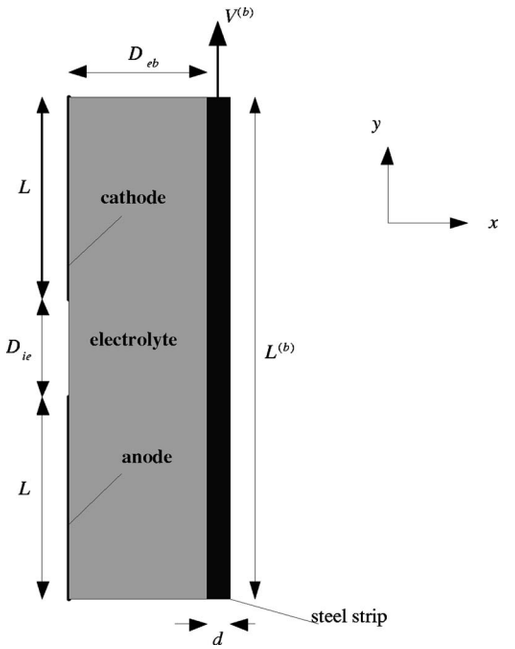

Figure 2. A cross section of the vertical model geometry for the Neograv pickling process showing the anode, the cathode, and the steel strip in the channel. The electrodes to the left are separated by an electrically insulated, impermeable boundary.

cases are somewhat simpler than for the electrolytic pickling process. In order to fix ideas, we focus in Fig. 1 on what is conceptually the simpler part of the process, i.e., where the steel strip is moving upward. Here, the motion of the strip can be expected to complement buoyancy forces in the removal of bubbles from the surface of the steel strip; where the strip moves downward, these two effects can be expected to counteract each other. The model we present in this paper includes the major electrochemical reactions, namely for hydrogen and oxygen bubble evolution and surface oxide removal, and bulk reactions, as well as the upward motion of the strip.

Problem Definition

We focus on a two-dimensional region of length $L^{(b)}$ and width $D_{eb} + d$, as shown in Fig. 2. At $x = 0$, there are anode and cathode electrodes, each of length L, that are a distance D_{ie} apart. On the right side of this region is a steel strip which moves vertically upward with speed $V^{(b)}$ and which is at a horizontal distance D_{eb} from the electrodes. Because of symmetry, only one half of the electrode–steel strip section is modeled; thus, d denotes the half-width of the steel strip, so that the center line of the strip lies at $x = D_{eb} + d$. We consider a potentiostatic problem where the potential difference between the anode and cathode is U. The remainder of the boundary at $x = 0$ is assumed to be impermeable and insulated. Characteristic values for D_{eb}, D_{ie}, d, L, $L^{(b)}$, U, and $V^{(b)}$, based on those for the actual Neograv process, are given in Table I.

Electrochemical modeling.— The electrochemical reactions considered in the model are hydrogen evolution at the cathode and cathodic sections of the steel strip, given by

$$2H_2O + 2e^- \rightarrow H_2 + 2OH^- \quad [1]$$

oxygen evolution at the anode and anodic sections of the steel strip, given by

$$2H_2O \rightarrow O_2 + 4H^+ + 4e^- \quad [2]$$

and chromium oxide dissolution at anodic sections of the steel strip, given by

Table I. Parameters used in the numerical analysis.

Parameter	Value	Units	Reference
a	6×10^{-5}	m	29 and 30
c_{H_2O}	55500	mol m^{-3}	32
$c_{Na_2SO_4}$	1197	mol m^{-3}	—
d	0.8×10^{-3}	m	—
$D_{Cr_2O_7^{2-}}$	1.13×10^{-9}	m^2 s^{-1}	[a]
D_{H^+}	9.31×10^{-9}	m^2 s^{-1}	21
D_{Na^+}	1.33×10^{-9}	m^2 s^{-1}	21
D_{OH^-}	5.26×10^{-9}	m^2 s^{-1}	21
$D_{SO_4^{2-}}$	1.07×10^{-9}	m^2 s^{-1}	33
D_{eb}	0.04	m	—
D_{ie}	0.05	m	—
$D_{\parallel}$	8	—	27
$D_{\perp}$	1	—	27
E^{eq}_{0,H_2}	−0.828	V	21
E^{eq}_{0,O_2}	1.23	V	21
$\kappa^{(b)}$	10^7	S m^{-1}	33
L	0.475	m	—
$L^{(b)}$	1	m	—
$M_{Cr_2O_3}$	0.152	kg mol^{-1}	33
M_{H_2}	0.002	kg mol^{-1}	33
M_{O_2}	0.032	kg mol^{-1}	33
T	298	K	—
U	20	V	—
$V^{(b)}$	1	m s^{-1}	—
$\mu_{Na_2SO_4^{2-}}$	1.5×10^{-3}	kg m^{-1} s^{-1}	33
$\rho_{Cr_2O_3}$	5220	kg m^{-3}	33
ρ_{H_2}	0.090	kg m^{-3}	33
$\rho_{Na_2SO_4^{2-}}$	1133.06	kg m^{-3}	33
ρ_{O_2}	1.429	kg m^{-3}	33
$\rho_{Na_2SO_4^{2-}}$	0.076	N m^{-1}	33

[a] The value for $D_{Cr_2O_7^{2-}}$ is unavailable in literature; instead, the value for $D_{CrO_4^{2-}}$ from Lide[32] was used for the computations.

$$Cr_2O_3 + 4H_2O \rightarrow Cr_2O_7^{2-} + 8H^+ + 6e^- \quad [3]$$

Although other oxides are undoubtedly present, earlier work[1] would suggest that chromium oxide is the one that predominates, which is why we include it in the model ahead of any others.

The most important homogeneous bulk reaction is assumed to be the water autoprotolysis reaction, given by

$$H_2O \rightleftharpoons H^+ + OH^- \quad [4]$$

Ipek et al.[14] also considered the dissociation of sulfuric acid, according to

$$H_2SO_4 \rightleftharpoons H^+ + HSO_4^-$$

$$HSO_4^- \rightleftharpoons H^+ + SO_4^{2-}$$

but we omit it here for two reasons: its inclusion in a single-phase model did not lead to significant differences with respect to the current density; further, its inclusion was found to lead to overexcessive computation times in the subsequent numerical modeling. Consequently, five ionic species are considered in the analysis: H^+, OH^-, SO_4^{2-}, $Cr_2O_7^{2-}$, and Na^+.

Three mechanisms, diffusion, migration, and convection, are assumed to contribute to the transport of ionic species in the electrolyte. Assuming the applicability of transport equations in dilute solutions (see, e.g., Ref. 21), the molar flux, $\mathbf{N}_i$, of the ionic species i can be expressed via the Nernst–Planck equation as

$$\mathbf{N}_i = c_i\mathbf{u} - D_i\nabla c_i - \frac{z_i F c_i D_i}{RT}\nabla\Phi^{(e)}, \quad i = 1, \ldots, N \quad [5]$$

where c_i denotes the concentration of species i and $\Phi^{(e)}$ is the electric potential in the electrolyte. $\mathbf{u}$ is the velocity of the electrolyte, D_i

is the diffusion coefficient, and z_i the charge number for species i. The quantities F, R, and T are Faraday's constant, the universal gas constant, and the absolute temperature, respectively. More generally, ionic activities rather than concentrations should be used, so that using Eq. 5 is an approximation.

The presence of bubbles in the electrolyte is expected to modify the diffusivity and thus the conductivity of the mixture. A common approach, investigated by Tobias and co-workers,[22-24] and implemented more recently by Wedin and Dahlkild[17] and Mat et al.,[18] is to use the Bruggeman correlation[25] for the diffusion coefficient and the mobility of species, so that Eq. 5 is replaced by

$$\mathbf{N}_i = c_i(1-\gamma)\mathbf{u} - D_i(1-\gamma)^{3/2}\nabla c_i - \frac{z_i F c_i D_i}{RT}(1-\gamma)^{3/2}\nabla\Phi^{(e)} \quad [6]$$

where γ is the gas volume fraction. The differential material balance for species i is given, in steady state, by

$$\nabla \cdot \mathbf{N}_i = R_i, \quad i = 1, \ldots, N \quad [7]$$

where R_i represents the production of species i through chemical reactions in the electrolyte. To compensate for the presence of the gas phase, the differential material balance for species i in steady state is taken as

$$\nabla \cdot \mathbf{N}_i = (1-\gamma)R_i, \quad i = 1, \ldots, N \quad [8]$$

Here, we have modified the reaction term, because bulk reactions can occur only where electrolyte is actually present. In addition, the solution is electrically neutral, except for a thin electrochemical double layer adjacent to the electrodes and steel strip surface. The condition of electroneutrality states that

$$\sum_{i=1}^{N} z_i c_i = 0 \quad [9]$$

The $N + 1$ equations presented above, i.e., Eq. 8 and 9, then provide a consistent description of transport processes in dilute electrolytic solutions. In addition, the current density $\mathbf{i}$ in an electrolytic solution is calculated from the flux of charged species and is given by Faraday's law as

$$\mathbf{i} = F\sum_{i=1}^{N} z_i \mathbf{N}_i \quad [10]$$

where F is Faraday's constant.

Hydrodynamical two-phase modeling.— Oxygen and hydrogen bubble evolution at the electrode and the steel strip surfaces necessitates that we model the natural convection of a bubbly two-phase flow. For simplicity, we assume that the flow is laminar and adopt the approach of Wedin and Dahlkild,[17] which is in turn based on the mixture-model formulation of two-phase flow according to Ishii and Zuber.[26] We briefly review the theory here.

The bubble-electrolyte mixture is assumed to behave like a homogeneous Newtonian fluid. The gas density ρ_D, and its dynamic viscosity μ_D, are assumed to be negligible compared to the density ρ_C and viscosity μ_C of the electrolyte, respectively. Both the effective density ρ and the viscosity μ of the gas–fluid mixture depend on the local volume fraction of bubbles, γ, according to

$$\rho = \gamma\rho_D + (1-\gamma)\rho_C \approx (1-\gamma)\rho_C$$

$$\mu = \mu_C\left(1 - \frac{\gamma}{\gamma_m}\right)^{-2.5(\mu_D+0.4\mu_C/\mu_D+0.4\mu_C)\gamma_m} \approx \frac{\mu_C}{1-\gamma}$$

The subscripts D and C denote the dispersed and continuous phases, respectively. For simplicity, we assume the volume fraction for maximum packing, γ_m, to be equal to 1. If now $\mathbf{u}_D$ and $\mathbf{u}_C$ are the separate velocities of the two phases, we can write the superficial velocities (the averaged velocity based on the net flux of the phases) as

$$\mathbf{j}_D = \gamma\mathbf{u}_D \quad [11]$$

$$\mathbf{j}_C = (1-\gamma)\mathbf{u}_C \quad [12]$$

giving a volume-averaged velocity for the mixture $\mathbf{j}$ as

$$\mathbf{j} = \mathbf{j}_D + \mathbf{j}_C \quad [13]$$

Introducing the mass-averaged velocity $\mathbf{u}$ for the mixture by

$$\rho\mathbf{u} = \rho_D\mathbf{j}_D + \rho_C\mathbf{j}_C \quad [14]$$

and the relative volume flux density vector $\mathbf{j}_r$ as

$$\mathbf{j}_r = \mathbf{j}_D - \gamma\mathbf{j} \quad [15]$$

we can, in the limit $\rho_C \gg \rho_D$, express the relation between $\mathbf{j}$ and $\mathbf{u}$ as

$$\mathbf{j} = \mathbf{u} + \frac{\mathbf{j}_r}{1-\gamma} \quad [16]$$

Constitutive closure laws, based on empirical relations developed for sedimenting spherical particles of radius a, are then proposed for $\mathbf{j}_r$ to give the motion of the monodisperse gas phase relative to the mixture. In particular, $\mathbf{j}_r$ is written as

$$\mathbf{j}_r = \mathbf{j}_S + \mathbf{j}_{\text{diff}} + \mathbf{j}_{\text{shear}} \quad [17]$$

where

$$\mathbf{j}_S = \gamma U_S f(\gamma)\mathbf{e}_y \quad [18]$$

$$\mathbf{j}_{\text{diff}} = -aU_S f(\gamma)\left[D_\perp\frac{\partial\gamma}{\partial x}\mathbf{e}_x + D_\parallel\frac{\partial\gamma}{\partial y}\mathbf{e}_y\right] \quad [19]$$

$$\mathbf{j}_{\text{shear}} = -a^2\left|\frac{\partial v}{\partial x}\right|\beta(\gamma)\nabla\gamma \quad [20]$$

The physical meaning of each of these terms, which are for the most part based on the mutual interactions between bubbles, is as follows.

1. $\mathbf{j}_S$: The rise of a single bubble can be described in terms of the Stokes terminal rise velocity, $U_S = ga^2\rho_C/3\mu_C$. The hindering effects induced by neighboring bubbles at higher volume fractions are accounted for by means of the hindered velocity function

$$f(\gamma) = (1-\gamma)^2$$

which assumes that the bubbles rise with the velocity of a single bubble, as modified by the effective velocity and density of the mixture. The vertical relative volume flux density $\mathbf{j}_S$ directly caused by buoyancy is then given by Eq. 18.

2. $\mathbf{j}_{\text{diff}}$: With the assumption that bubbles at small bubble Reynolds numbers move with the same irregular motion as settling particle suspensions, we consider the hydrodynamic self-diffusion, $\mathbf{j}_{\text{diff}}$ as described in Eq. 19. The magnitude of this process is greater in the direction parallel to the rising gas bubbles, which is represented by the respective magnitudes of the diffusion coefficients, $D_\perp$ and $D_\parallel$: $D_\perp \approx 1$ and $D_\parallel \approx 8$; for more details, see Ref. 27.

3. $\mathbf{j}_{\text{shear}}$: This is due to the process of shear-induced hydrodynamic diffusion and is given by Eq. 20, in which $\beta(\gamma)$ is an empirical function valid for $\gamma < 0.5$ and given by Leighton and Acrivos[28] as

$$\beta(\gamma) = \frac{\gamma^2}{3}[1 + 0.5\exp(8.8\gamma)] \quad [21]$$

The diffusion process is assumed to be caused by the interactions of particles with an average displacement a and an interaction frequency which is proportional to the magnitude of the shear rate, $|\partial v/\partial x|$.

In summary, the terms in Eq. 17 describe the average transport of bubbles relative to the liquid and the transport away from the walls where they are produced. In the immediate vicinity of these walls, within distances on the order of a bubble diameter, the mechanisms

described above have to be modified because of interactions with the wall and the bubbles that adhere to it. However, the influence of these details on the main flow is neglected here.

Even though all of the empirical functions mentioned above were originally developed for small particles, it is a reasonable assumption that they are also valid for small bubbles, due to stiffening of the bubble surfaces by impurities; for a further discussion of this, see Wedin and Dahlkild.[17] A further issue is whether or not the assumption that the bubbles remain spherical is reasonable. For hydrogen bubbles, Vogt[29] gives a value for a of 25 μm, which implies that the bubble Reynolds number, Re_{2a}, defined by

$$Re_{2a} = 2aU_S\rho_C/\mu_C \quad [22]$$

and the Weber number, given by

$$We_{2a} = 2aU_S^2\rho_C/\sigma_C \quad [23]$$

are both much smaller than unity; Ipek et al.[13] calculate the values $Re_{2a} \approx 10^{-2}$, $We_{2a} \approx 10^{-6}$, so that the flow remains within the Stokes regime, and therefore the assumption is not unreasonable. For oxygen bubbles, the value for a given by Janssen et al.[30] (100 μm) leads to $Re_{2a} \approx 1$, $We_{2a} \approx 10^{-3}$, which is on the margins of the Stokes flow regime. In addition, we do not take account of bubble coalescence, neither do we differentiate between oxygen and hydrogen bubbles, i.e., we use a common value for the bubble radius, a, and thus the Stokes terminal rise velocity, which is the average of the values given by Vogt[29] and Janssen et al.[30] Also, the bubble diameter change as the bubble rises is not accounted for, as the pressure difference between the bottom and the top of the cell is small compared to the ambient pressure. Other contributing transport mechanisms could be considered, such as wall-interaction effects, migration caused by bubble rotation, and possible migration due to electrically charged impurities on the bubble skin; all of these are beyond the present scope.

Derivation of the Model Equations

The model equations are derived from the transport equations and electrode kinetics, described in the preceding section and in Ref. 14. The electrochemical model includes seven unknown variables: five concentrations, c_{H^+}, c_{OH^-}, $c_{SO_4^{2-}}$, $c_{Cr_2O_7^{2-}}$, and c_{Na^+}, and the potential fields in the electrolyte, $\Phi^{(e)}$, and the steel strip, $\Phi^{(b)}$. Consequently, six model equations need to be derived in the electrolyte and on its boundaries. One model equation is required within the steel strip and on its boundaries. The hydrodynamic model consists of four unknown variables: the x and y components of the velocity vector $\mathbf{u}$, u and v, respectively, the pressure p, and the gas fraction, γ; this requires four equations for the electrolyte.

Domain equations.— Inserting the expression for molar flux Eq. 6 into the material balance Eq. 8 yields

$$\nabla \cdot [(1-\gamma)\mathbf{u}c_i] = D_i\nabla \cdot [(1-\gamma)^{3/2}\,\nabla\, c_i] + \frac{z_iFD_i}{RT}\nabla \cdot [c_i(1-\gamma)^{3/2}\nabla\Phi^{(e)}] + (1-\gamma)R_i \quad [24]$$

for each ionic species i. The production rate R_i for each of the species is as given by Ipek et al.[14] For later use, we note that we can sum the species conservation equations to give

$$\nabla \cdot \left[\frac{F^2}{RT}\sum_{i=1}^{N=5} z_i^2(1-\gamma)^{3/2}D_ic_i\nabla\Phi^{(e)}\right] + \nabla \cdot \left[F\sum_{i=1}^{N=5} z_i(1-\gamma)^{3/2}D_i\nabla c_i\right] = 0 \quad [25]$$

where we identify the index i with each of the ionic species according to

$$1 \Leftrightarrow H^+, \quad 2 \Leftrightarrow OH^-, \quad 3 \Leftrightarrow SO_4^{2-}, \quad 4 \Leftrightarrow Cr_2O_7^{2-}, \quad 5 \Leftrightarrow Na^+$$

For the potential field in the steel strip, we have

$$\nabla^2\Phi^{(b)} = 0 \quad [26]$$

The governing equations for $\mathbf{u}$, P, and γ in the electrolyte are

$$\nabla \cdot [(1-\gamma)\mathbf{u}] = 0 \quad [27]$$

$$\nabla \cdot \left(\gamma\mathbf{u} + \frac{\mathbf{j}_r}{1-\gamma}\right) = 0 \quad [28]$$

$$\rho_C(1-\gamma)\mathbf{u} \cdot \nabla\mathbf{u} = \gamma\rho_C g\mathbf{e}_y - \nabla P + \nabla \cdot \left\{\frac{\mu_C}{1-\gamma}\left[\nabla\mathbf{u} + (\nabla\mathbf{u})^T - \tfrac{2}{3}\nabla \cdot \mathbf{u}\right]\right\} \quad [29]$$

where P is related to the actual pressure p by

$$P = p + \rho_C g y \quad [30]$$

Electrochemical boundary conditions.— In what follows, we consider a potentiostatic system and set the anode and cathode potentials to $\pm U/2$, respectively. At the anode surface, we have

$$\mathbf{N}_{H^+} \cdot \mathbf{n} = \frac{(1-\gamma)i_{O_2}}{F} \quad [31]$$

$$\mathbf{N}_{OH^-} \cdot \mathbf{n} = 0 \quad [32]$$

$$\mathbf{N}_{SO_4^{2-}} \cdot \mathbf{n} = 0 \quad [33]$$

$$\mathbf{N}_{Cr_2O_7^{2-}} \cdot \mathbf{n} = 0 \quad [34]$$

$$\mathbf{N}_{Na^+} \cdot \mathbf{n} = 0 \quad [35]$$

where

$$i_{O_2} = i_{0,O_2}^{(a)} \exp\left[\frac{\alpha_{O_2}^{(a)}F(U/2 - \Phi^{(e)} - E_{O_2}^{eq})}{RT}\right] \quad [36]$$

Similarly, at the cathode surface

$$\mathbf{N}_{H^+} \cdot \mathbf{n} = 0 \quad [37]$$

$$\mathbf{N}_{OH^-} \cdot \mathbf{n} = -\frac{(1-\gamma)i_{H_2}}{F} \quad [38]$$

$$\mathbf{N}_{SO_4^{2-}} \cdot \mathbf{n} = 0 \quad [39]$$

$$\mathbf{N}_{Cr_2O_7^{2-}} \cdot \mathbf{n} = 0 \quad [40]$$

$$\mathbf{N}_{Na^+} \cdot \mathbf{n} = 0 \quad [41]$$

where

$$i_{H_2} = -i_{0,H_2}^{(c)} \exp\left[-\frac{\alpha_{H_2}^{(c)}F(-U/2 - \Phi^{(e)} - E_{H_2}^{eq})}{RT}\right] \quad [42]$$

Note that in Eq. 31 and 38, in order to take account of the reduction of electrode surface area due to blockage by bubbles, we use the approach of Dahlkild[16] and Wedin and Dahlkild,[17] among others, and introduce a multiplicative factor $(1-\gamma)$ for the current density.

The steel strip acts as a bipolar electrode, and therefore the Tafel equations for oxygen and hydrogen evolution at the corresponding sections are implemented. In particular, the normal component of the current density, $i^{(b)} := \mathbf{i} \cdot \mathbf{n}$, at the steel strip/electrolyte interface is taken as

$$i^{(b)} = \begin{cases} (1-\gamma)i_{H_2} & \text{if } \Phi^{(b)} - \Phi^{(e)} \leqslant E^{eq}_{0,H_2} \\ 0 & \text{if } E^{eq}_{0,H_2} \leqslant \Phi^{(b)} - \Phi^{(e)} \leqslant E^{eq}_{0,O_2} \\ (1-\gamma)(i_{Cr_2O_3} + i_{O_2}) & \text{if } \Phi^{(b)} - \Phi^{(e)} \geqslant E^{eq}_{0,O_2} \end{cases} \quad [43]$$

where

$$i_{O_2} = i^{(b)}_{0,O_2} \exp\left[\frac{\alpha^{(b)}_{O_2} F}{RT}(\Phi^{(b)} - \Phi^{(e)} - E^{eq}_{O_2})\right] \quad [44]$$

$$i_{Cr_2O_3} = \left(\frac{\Lambda}{1-\Lambda}\right) i_{O_2} \quad [45]$$

$$i_{H_2} = -i^{(b)}_{0,H_2} \exp\left[-\frac{\alpha^{(b)}_{H_2} F}{RT}(\Phi^{(b)} - \Phi^{(e)} - E^{eq}_{H_2})\right] \quad [46]$$

These are used to give the following boundary conditions at the steel strip/electrolyte interface

$$\mathbf{N}_{H^+} \cdot \mathbf{n} = (1-\gamma)\left(\frac{i_{O_2}}{F} + \frac{4i_{Cr_2O_3}}{3F}\right) \quad [47]$$

$$\mathbf{N}_{OH^-} \cdot \mathbf{n} = -\frac{(1-\gamma)i_{H_2}}{F} \quad [48]$$

$$\mathbf{N}_{SO_4^{2-}} \cdot \mathbf{n} = 0 \quad [49]$$

$$\mathbf{N}_{Cr_2O_7^{2-}} \cdot \mathbf{n} = \frac{(1-\gamma)i_{Cr_2O_3}}{6F} \quad [50]$$

$$\mathbf{N}_{Na^+} \cdot \mathbf{n} = 0 \quad [51]$$

Further details on the derivation of these boundary conditions are given in Ref. 14.

Continuity of the normal current at the steel strip/electrolyte interface gives the boundary condition

$$\begin{aligned} &\kappa^{(b)} \nabla \Phi^{(b)} \cdot \mathbf{n} \\ &\quad = F \sum_{i=1}^{5} z_i \mathbf{N}_i \cdot \mathbf{n} \\ &\quad = (1-\gamma)\left[z_{OH^-} i_{H_2} + \frac{1}{6} z_{Cr_2O_7^{2-}} i_{Cr_2O_3} + z_{H^+}\left(i_{O_2} + \frac{4i_{Cr_2O_3}}{3}\right)\right] \end{aligned} \quad [52]$$

Note, finally, that Eq. 47-52 constitute six equations in seven unknowns, but that a seventh equation comes from the electroneutrality condition.

At the inlet at $y = 0$, the concentrations must be such that there is local equilibrium, so we set

$$c_i = c_i^{eq} \quad [53]$$

The values of these are given in Table III in Ipek et al.,[14] as are details of their derivation; in addition, the normal component of the current is set to zero

$$\mathbf{i} \cdot \mathbf{n} = 0 \quad [54]$$

which can be reduced to

$$\nabla \Phi^{(e)} \cdot \mathbf{n} = 0 \quad [55]$$

Note here that the values of c_i^{eq} in Eq. 53 give an indication of the extent of the validity of the assumption regarding the use of dilute electrolyte theory for the bulk electrolyte. As indicated by Newman and Thomas-Alyea[21] (chap. 12, p. 305), the equations for the dilute theory can be derived from the concentrated theory if

$$c_i \ll c_0$$

where c_0 is the solvent concentration, in this case that of water. As a measure of the dilution, consider $\Sigma c_i / c_{H_2O}$, where the sum is taken over the ionic species only. Using Tables I and III from Ipek et al.,[14] we have that, in the bulk electrolyte

$$\frac{\Sigma c_i}{c_{H_2O}} \approx 0.065$$

We discuss the corresponding value in the boundary layers later.

At the outlet boundary, we assume that for all ionic species the convective flux in the axial direction of the channel is dominant. Consequently, we set the sum of the diffusive and migrative fluxes to zero

$$\left(-D_i \nabla c_i - \frac{z_i F c_i D_i}{RT} \nabla \Phi^{(e)}\right) \cdot \mathbf{n} = 0, \quad i = 1, \ldots, 5 \quad [56]$$

Combining this with the electroneutrality condition, we obtain

$$\nabla c_i \cdot \mathbf{n} = 0, \quad i = 1, \ldots, 5 \quad [57]$$

and

$$\nabla \Phi^{(e)} \cdot \mathbf{n} = 0 \quad [58]$$

At the boundary of the electrolyte domain that is assumed to be insulated, i.e., $x = 0$, $L \leqslant y \leqslant L + D_{ie}$, we have

$$\mathbf{N}_i \cdot \mathbf{n} = 0, \quad i = 1, \ldots, 5 \quad [59]$$

Similarly, at the boundaries of the steel strip, which are either symmetry planes or insulated, we have

$$\nabla \Phi^{(b)} \cdot \mathbf{n} = 0 \quad [60]$$

Hydrodynamic boundary conditions.— Combining Eq. 13 and 15, we obtain

$$\mathbf{j}_r \cdot \mathbf{n} = (1-\gamma) j_D$$

where j_D (with dimensions m s^{-1}) is given from Faraday's law by

$$j_D = \left(\frac{M_D}{z_D F \rho_D}\right) \mathbf{i} \cdot \mathbf{n}$$

where z_D is the number of electrons participating in the gas-evolving reaction, M_D is the molar weight of the gas, i.e., the disperse phase, and ρ_D is its density. Furthermore, because $\rho_C \gg \rho_D$, Eq. 14 is well-approximated by

$$\mathbf{u} \cdot \mathbf{n} = \frac{\rho_D j_D}{\rho_C (1-\gamma)}$$

These considerations are implemented on the various reaction interfaces as follows.

At the anode

$$u = \frac{\rho_{O_2} j_{O_2}}{\rho_C (1-\gamma)}, \quad v = 0, \quad \mathbf{j}_r \cdot \mathbf{n} = (1-\gamma) j_{O_2} \quad [61]$$

where

$$j_{O_2} = \left(\frac{M_{O_2}}{4F\rho_{O_2}}\right) i^{(a)}_{0,O_2} \exp\left[\frac{\alpha^{(a)}_{O_2} F (U/2 - \Phi^{(e)} - E^{eq}_{O_2})}{RT}\right]$$

At the cathode

$$u = \frac{\rho_{H_2} j_{H_2}}{\rho_C (1-\gamma)}, \quad v = 0, \quad \mathbf{j}_r \cdot \mathbf{n} = (1-\gamma) j_{H_2} \quad [62]$$

where

$$j_{H_2} = \left(\frac{M_{H_2}}{2F\rho_{H_2}}\right) i^{(c)}_{0,H_2} \exp\left[-\frac{\alpha^{(c)}_{H_2} F (-U/2 - \Phi^{(e)} - E^{eq}_{H_2})}{RT}\right]$$

On the steel strip surface at $x = D_{eb}$, we have

$$u = \frac{\rho_D j_D}{\rho_C(1-\gamma)}, \quad v = V, \quad \mathbf{j}_r \cdot \mathbf{n} = (1-\gamma) j_D \tag{63}$$

where

$$j_D = \left(\frac{M_{O_2}}{4F\rho_{O_2}}\right) i_{0,O_2}^{(b)} \exp\left[\frac{\alpha_{O_2}^{(b)} F(\Phi^{(b)} - \Phi^{(e)} - E_{O_2}^{eq})}{RT}\right] + \left(\frac{M_{H_2}}{2F\rho_{H_2}}\right) i_{0,H_2}^{(b)} \exp\left[-\frac{\alpha_{H_2}^{(b)} F(-\Phi^{(b)} - \Phi^{(e)} - E_{H_2}^{eq})}{RT}\right]$$

At the inlet at $y = 0$, we set a linear Couette profile

$$u = 0, \quad v = \frac{V^{(b)} x}{D_{eb}} \tag{64}$$

This was the assumed profile for the entire geometry for the earlier single-phase model,[14] but it seems a logical step to restrict it to the inlet in a two-phase model. In addition, we can reasonably assume that there is no gas phase present at the inlet, so we take

$$\gamma = 0 \tag{65}$$

At the outlet, the pressure is constant and the flow is assumed to be fully developed, so we set

$$P = 0, \quad \nabla v \cdot \mathbf{n} = 0, \quad \nabla \gamma \cdot \mathbf{n} = 0 \tag{66}$$

At the remaining boundary, i.e., $x = 0$, $L \leq y \leq L + D_{ie}$, we set no slip for the velocity field, so that

$$u = 0, \quad v = 0 \tag{67}$$

This, combined with the fact that gas cannot pass through the impermeable surface, gives

$$\nabla \gamma \cdot \mathbf{n} = 0 \tag{68}$$

Numerical Implementation

The numerical problem to be solved consists of the solution to (*i*) the electrochemical model, Eq. 9, 24, and 26, subject to boundary conditions 31-35, 37-41, 47-54, 56, 59, and 60; (*ii*) the hydrodynamical model, Eq. 27-29, subject to boundary conditions 61-68.

It is clear that these are fully coupled, both through governing equations and boundary conditions, and must be solved for simultaneously. In this paper, we solve the two models detailed in appendices A and B in Ipek et al.,[14] which were termed there as reduced models 1 and 2; these both include seven unknown variables, namely, c_{H^+}, c_{OH^-}, $c_{SO_4^{2-}}$, $c_{Cr_2O_7^{2-}}$, c_{Na^+}, $\Phi^{(e)}$, and $\Phi^{(b)}$, but differ from each other in that model 1 includes no bulk reactions, whereas model 2 include the water autoprotolysis reaction. The problem was solved numerically using the finite element-based PDE software, Comsol Multiphysics.[31] All computations were performed on a Dual AMD Opteron 242 computer with a 1.6 GHz processor and 4 GB memory.

Many of the details of the numerical implementation, in particular with regard to the resolution of the reaction layers and the use of artificial diffusion for stabilizing the solution of the electrochemical model, have already been given earlier for single-phase flow[14] and are not repeated here. Not surprisingly, the extension to two-phase flow gave even further implementation difficulties. A convenient strategy here was found to be to solve the hydrodynamic equations on a separate mesh that was coarser in the vicinity of the reacting surfaces than the one needed for the electrochemical model and to import the solution into the mesh used for the electrochemical equations; this is in view of the fact that the hydrodynamic boundary layer is considerably thicker than the electrochemical diffusion layer. In addition to the grid independence study carried out for the electrochemical-model equations,[14] a grid independence study was carried out for the hydrodynamical model equations also. Two different unstructured meshes, having approximately 100,000 and 150,000 elements and corresponding to 600,000 and 1 million degrees of freedom, respectively, were used. The relative differences between u, v, P, and γ for the two meshes were examined, and the difference in the average was found to be less than 0.1%. This justifies using the coarser of the two meshes, particularly in view of the lengthy computing times; for example, even when using the coarser mesh for the hydrodynamic equations, a typical computation for model 1 required a cumulative computation time of 10 CPU hours.

Results and Discussion

The first three subsections contain results obtained using the data in Table I. In the last two subsections, however, we vary U and $V^{(b)}$. In all cases, the X and Y labels on figure axes are related to the coordinates x and y by

$$X = \frac{x}{D_{eb}}, \quad Y = \frac{y}{L^{(b)}}$$

Potential and current density.— The potential fields in the electrolyte and in the steel strip and the corresponding current density vector **i** defined by

$$\mathbf{i} = \begin{cases} -\kappa^{(b)} \nabla \Phi^{(b)} \text{ in the strip,} \\ F \sum_{i=1}^{5} z_i \mathbf{N}_i \text{ in the electrolyte} \end{cases} \tag{69}$$

are qualitatively similar to those shown in Fig. 4a and b in Ipek et al.[14] and are therefore not shown here. Instead, we begin by showing, in Fig. 3a, the overpotential at the surface of the steel strip for models 1 and 2; Fig. 3b on the other hand shows the predicted current densities for these two models. As in the earlier work,[14] the differences are not particularly great, regardless of whether the water autoprotolysis bulk reaction is included or not, because the Tafel laws that are used to describe all of the electrode reactions do not contain ionic concentrations.

Also of interest are the overpotential and current density profiles at the surface of the steel strip; these are shown in Fig. 4 and 5, respectively, which show comparisons of results from the single- and two-phase models. Figure 5 indicates what might have been intuitively expected, i.e., that the local current density is lower when the gas phase is accounted for. However, Fig. 4 perhaps goes against expectation, because the magnitude of the overpotential is higher, even though the magnitude of the current density is lower; at the same time, this means that, for a given cell potential, the ohmic losses are lower. Nevertheless, ohmic losses still amount to slightly more than 60% of the cell voltage. Overall, the inclusion of two-phase flow gives a current density that is 10% lower than that for single-phase flow.

pH.— In the earlier work,[14] it was found that there were was little variation in the current density profiles at the steel strip between the various models, even though there were significant differences in the profiles of c_{H^+}, or equivalently the local pH; this turns out to be the case when a hydrodynamic two-phase model is used, although there are some additional observations.

Figure 6a shows the pH profile from model 1, where bulk reactions are omitted. Here, the pH is no higher than 7, the bulk value, and there are particularly acidic regions in the vicinities of both electrodes and the anodic part of the steel strip. Furthermore, the acidic zone near $X = 0$ extends for the whole length of the cell because of convective transport of H^+ ions produced at the anode and migration of H^+ ions towards the cathode. The significant difference between this figure and the corresponding one in Ipek et al.[14] is the thickness of the boundary layers near the electrodes; here, they are much thinner, a point we return to shortly.

Figure 6b shows the pH profile from model 2, where water autoprotolysis is accounted for. Here, the picture is considerably different, with low pH in the vicinity of the anode electrode, but high pH in the vicinity of the cathode; in addition, there is a thin layer of low pH near the anodic section of the steel strip. Also, adjacent to the cathodic section of the steel strip, an alkaline zone develops and

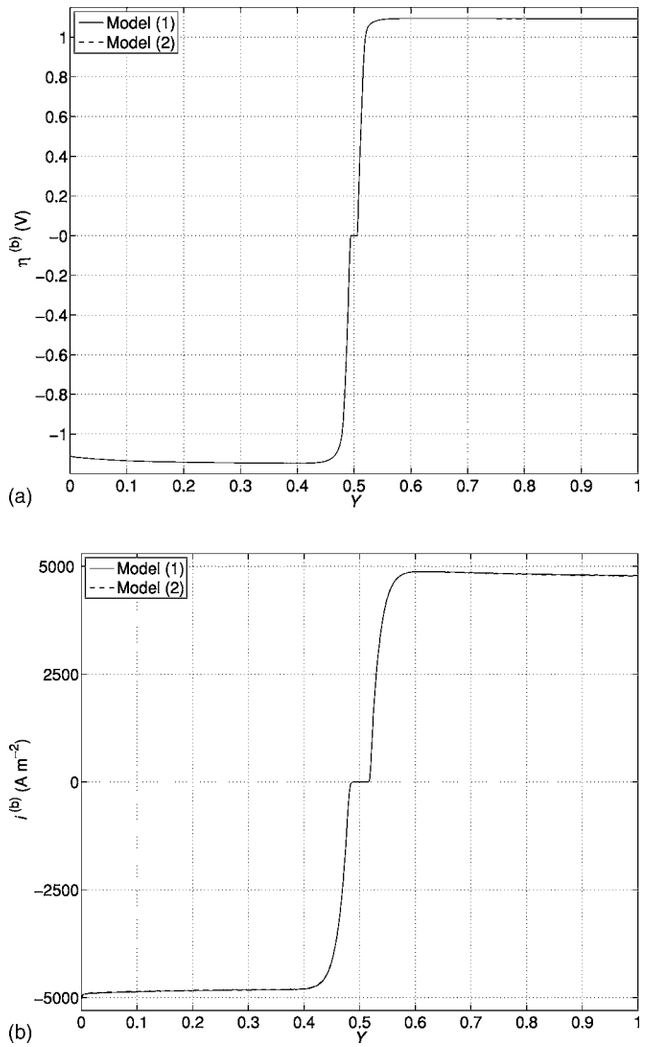

Figure 3. (a) Overpotential $\eta^{(b)}$ at the surface of the steel strip, and (b) current density $i^{(b)}$ at the surface of the steel strip.

extends along the length of the strip; this is analogous to the acidic zone near $X = 0$ mentioned in the previous paragraph and is due to the convective transport of OH^- ions produced at the strip. Overall, by comparison with Fig. 6a, it is clear that including the water autoprotolysis reaction in the model removes H^+ ions in those regions away from reacting surfaces where, in model 1, their concentration is high. Qualitatively, this figure is no different from the corresponding one for model 2 in Ipek et al.[14]

Further insight can be obtained by considering cross-sectional profiles for c_{H+} and pH; here, we look at profiles for $Y = 0.75$ between the cathode electrode and the anodic part of the steel strip surface. Figure 7a shows profiles for c_{H^+}, and is of use in seeing the differences in the thicknesses of the concentration boundary layers at the electrodes and the strip in each of the models. Most distinct is the comparatively thick layer in model 1 at the electrode. For single-phase flow,[14] its thickness was expected to scale as $Pe^{-1/3}$ ($\ll 1$), where Pe is the Péclet number, given by

$$Pe = \frac{V^{(b)} D_{eb}}{[D]}$$

with $[D]$ a characteristic ionic diffusion coefficient, typically of the order 10^{-9} m^2 s^{-1}, as indicated in Table I. Using the two-phase model, the concentration boundary layer is much thinner, presumably due to the enhanced convection as a result of the vertical bubble motion. At $X = 1$, the thickness of the concentration boundary layer is expected to scale as $Pe^{-1/2}$ for single-phase flow, because the steel strip is in motion with constant translational speed. In the two-phase flow, the thickness of this layer appears to be, qualitatively at least, unaltered. There are two plausible reasons for this: any enhanced convection there is much weaker than that due to the translational motion of the strip, and the current density at this surface is much lower than that at the electrodes, so we should not therefore expect as great a buoyancy effect. For model 2, we see that near $X = 0$, in addition to the boundary-layer structure mentioned already, there appears to be an inner layer also. This is best described as a reaction layer, where the diffusion term matches the production term in the species conservation equations. What happens for model 2 near $X = 1$ is rather unclear from this figure but becomes more distinct in Fig. 7b, which shows the pH profiles; the pH increases before falling to a value around 1 at the strip surface.

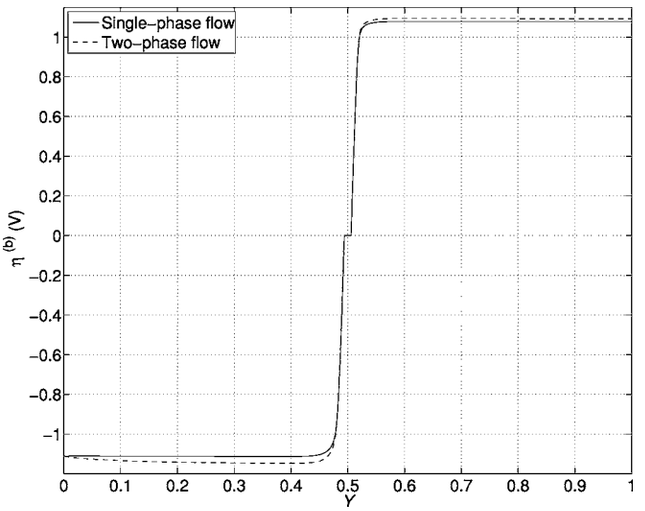

Figure 4. Comparison of overpotential $\eta^{(b)}$ at the surface of the steel strip for single- and two-phase flow with model 1.

Finally in this subsection, we return to the issue of how appropriate dilute electrolyte theory is for this flow. It is not possible to know a priori, as it was in the bulk, how valid the approximation

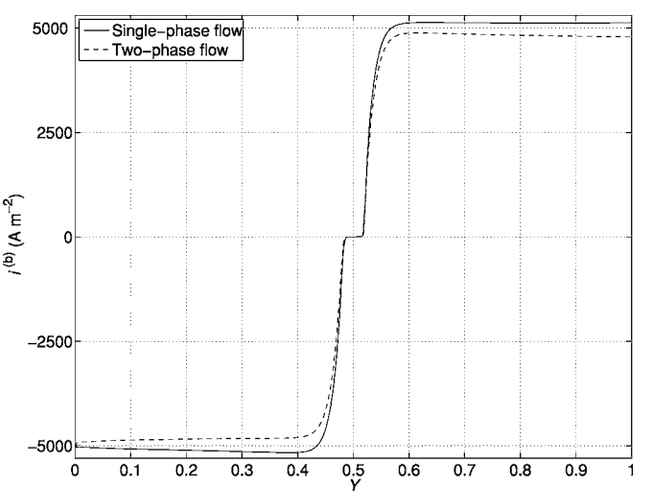

Figure 5. Comparison of current density $i^{(b)}$ at the surface of the steel strip for single- and two-phase flow with model 1.

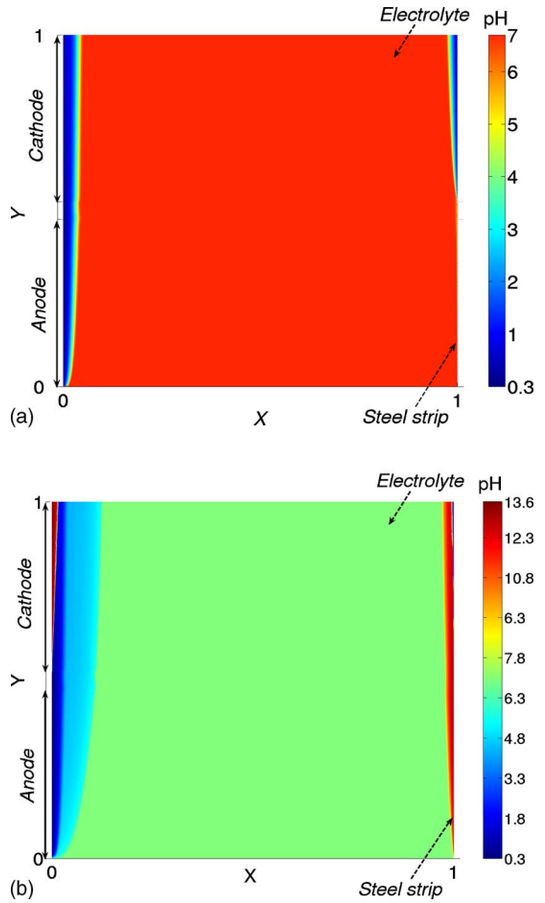

Figure 6. (Color online) pH profiles in the cell: (a) model 1 and (b) model 2.

will be in the boundary layers, because ionic species are being produced there. However, we have found from the computations that, for the base case

$$\frac{\Sigma c_i}{c_{\mathrm{H_2O}}} \leqslant 0.144$$

with the maximum value occurring at the cathode surface. This is roughly twice as high as the value in the bulk and clearly higher than desirable; an interesting future task will therefore be to implement concentrated electrolyte theory and to compare the results of the two.

Gas fraction and velocity distributions.— Figure 8 shows the gas fraction γ in the electrolyte. From this, it is clear that the bulk of the flow remains single phase, although there are boundary layers in γ along the vertical electrode and strip surfaces. Figures 9a and b show in more detail the behavior of γ at these vertical surfaces, at $X = 0$ and 1, respectively. On average, the values of γ are greater at the stationary boundary, $X = 0$, than at the moving boundary, $X = 1$; this is because more gas is being produced there, because the local current density is higher there and because it is not transported away as effectively. Also, the cusp in Fig. 9a is due to the sharp change in the boundary condition at the anode electrode and the insulated boundary at $X = 0$; the presence of this artificial insulated boundary also explains the subsequent drop in γ before the cathode electrode is reached. While this behavior is, to some extent, an artifact of the model, it is consistent with the general observation that there can be current density maxima at the edges of electrodes; in this model, it would mean enhanced local gas production, giving a sudden increase in γ, as is observed in Fig. 9a at $Y = 0.475$.

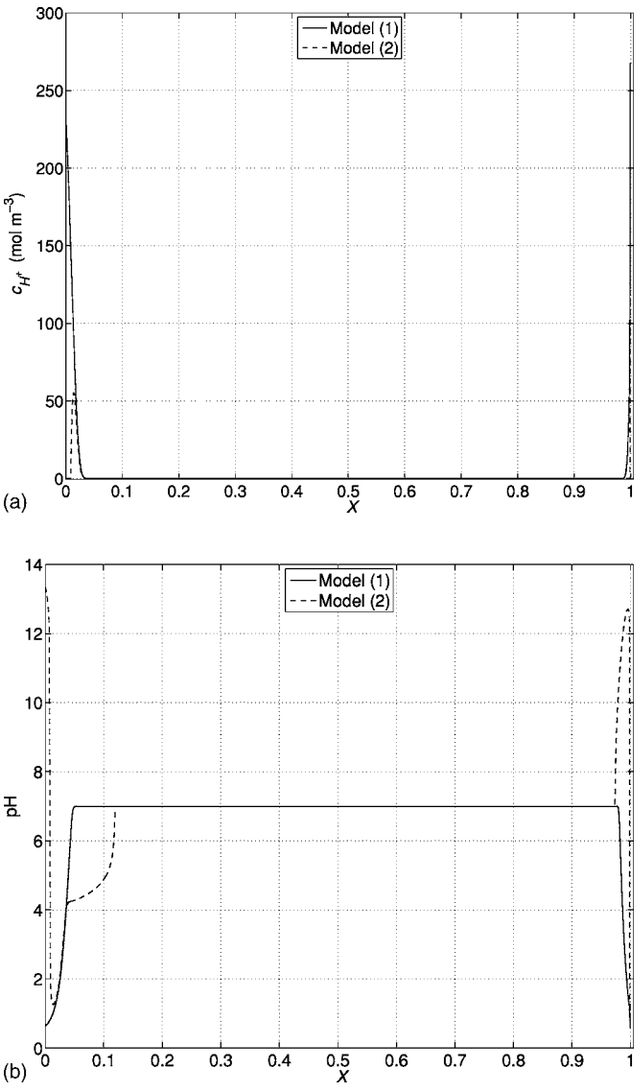

Figure 7. Cross-sectional profiles at $Y = 0.75$ for models 1 and 2 for (a) $c_{\mathrm{H+}}$ and (b) pH.

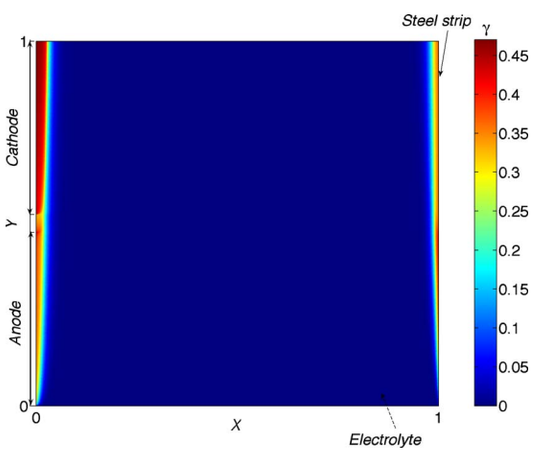

Figure 8. (Color online) Gas fraction γ in the electrolyte computed using the base-case parameters.

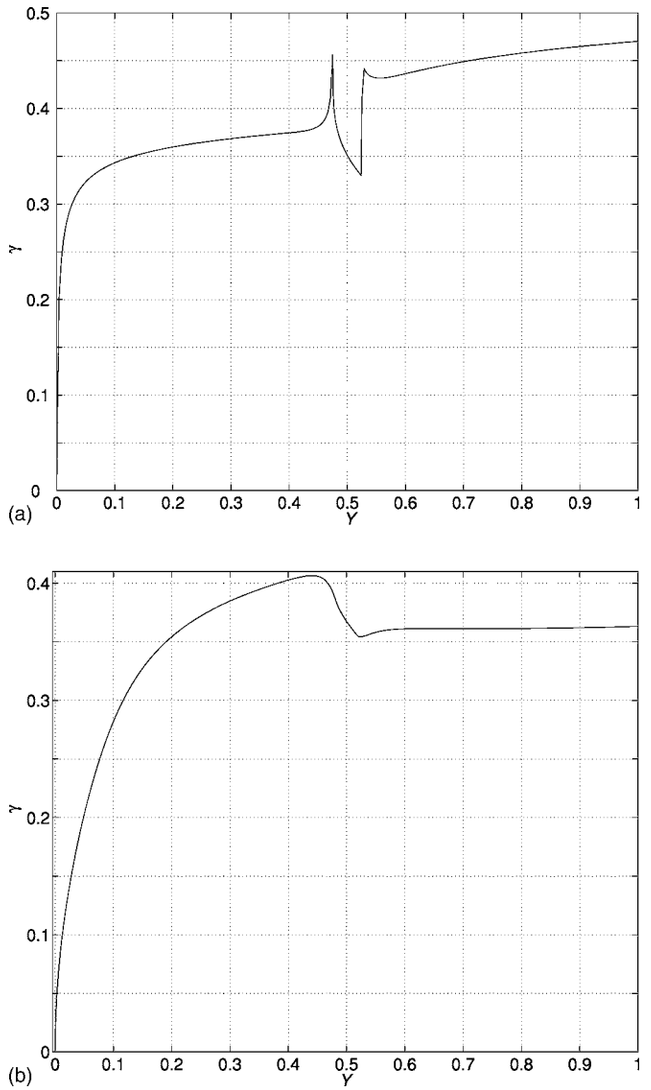

Figure 9. (a) Gas fraction γ at $X = 0$ (note that the artificial boundary between the anode and cathode electrodes for $0.475 < Y < 0.525$ is responsible for the unusual behavior of γ there); (b) gas fraction γ at $X = 1$ (steel strip).

Figure 10 shows the vertical component of the mixture velocity v at $Y = 0$, 0.25, 0.5, 0.75, and 1. In evidence here is the distortion of the Couette profile that was imposed at the inlet of the cell at $Y = 0$. This figure emphasizes the point made earlier about the enhanced convection due to the bubble generation at the vertical boundaries.

Effect of U and $V^{(b)}$.— Having established that the local current density profiles $i^{(b)}$ at the steel strip vary little regardless of the model used, we use the computationally less intensive model 1 to evaluate the effect of the strip speed $V^{(b)}$ and the cell potential U.

Figure 11 shows the effect of changes to the strip speed. Here, we see that a doubling of the speed from 0.5 to 1 m s^{-1} has little effect on the profiles, altering neither the qualitative form nor the quantitative values of the profiles. Figure 12 shows the effect of doubling the cell potential from 10 to 20 V. Here, the basic forms remain the same, although there is a distinct shift in the magnitude of the current density. Lastly, Fig. 13 summarizes the data in Fig. 11 and 12 by plotting the average current density at the steel strip $I^{(b)}$; we define this quantity as

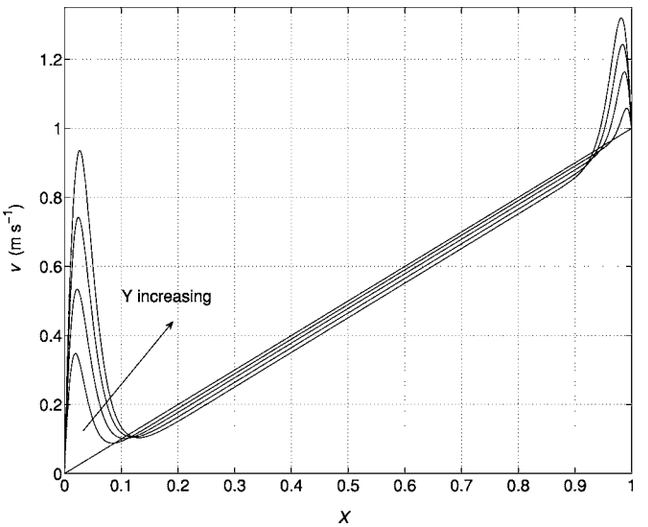

Figure 10. Vertical component velocity v at $Y = 0$, 0.25, 0.5, 0.75, and 1 computed using the base-case parameters (two-phase model).

$$I^{(b)} := \frac{1}{2}\int_0^1 |i^{(b)}|dY$$

Once again, it is clear that changes to $V^{(b)}$ in the interval from 0.5 to 1 m s^{-1} have little effect on cell performance.

Implications for chromium oxide scale removal.— The results of the model can subsequently be used to determine how much scale is removed from a given location on the strip; this was shown to be[14]

$$\delta_{Cr_2O_3} = \frac{M_{Cr_2O_3}L^{(b)}\Lambda I^{(b)}}{6(1+\Lambda)\rho_{Cr_2O_3}FV^{(b)}} \quad [70]$$

where $\delta_{Cr_2O_3}$ is the thickness of the scale removed. Figure 14 shows this as a function of $V^{(b)}$ for different values of cell potential for both the single- and two-phase models. From this, we see the lower strip

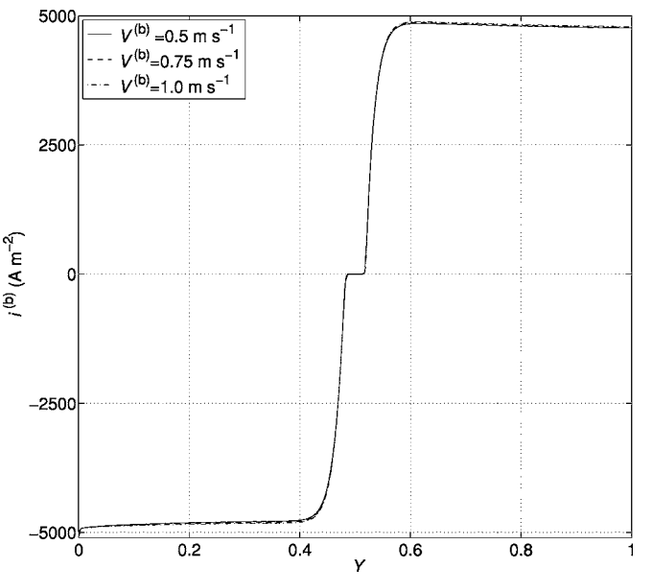

Figure 11. $i^{(b)}$ vs Y for model 1, for three different strip speeds, $V^{(b)}$, at $U = 20$ V (two-phase model).

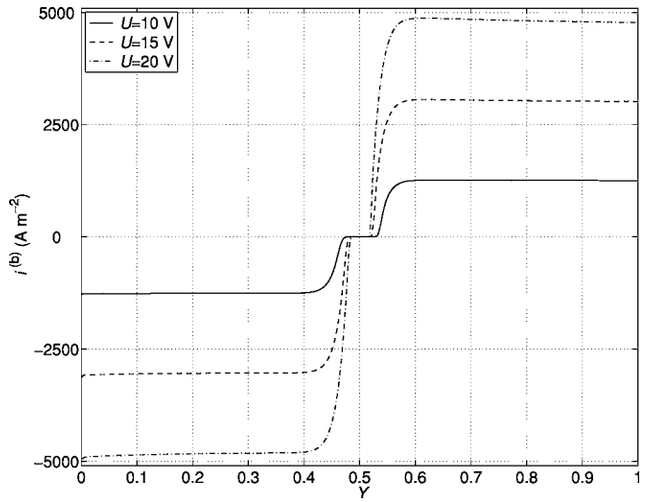

Figure 12. $i^{(b)}$ vs Y for model 1, for three different cell potentials, U, at $V^{(b)} = 1$ m s^{-1} (two-phase model).

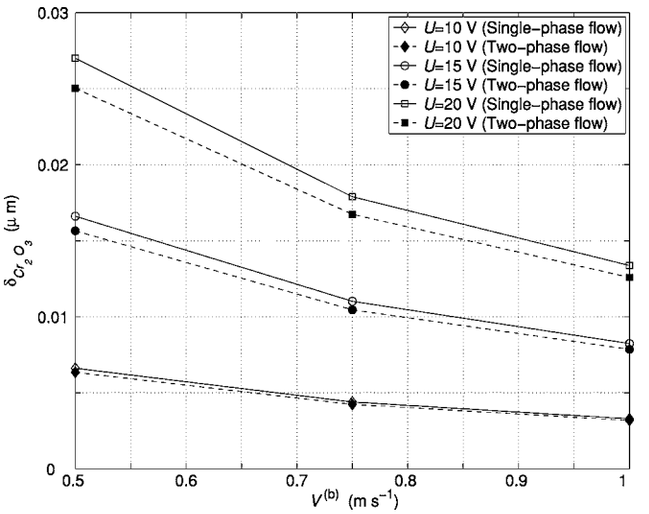

Figure 14. $\delta_{Cr_2O_3}$ vs $V^{(b)}$ for model 1, for three cell potentials, U (single- and two-phase models).

velocities clearly favor scale removal, as do higher cell potentials. In addition, the two-phase model shows that less scale is removed. Prior to obtaining these results, and as was surmized earlier,[14] one might have expected the possibility of greater complexity in the curves for two-phase flow, as compared to the curves for single-phase flow: at a combination of low strip speeds and high cell potentials, there could be a buildup of bubble coverage leading to inefficient scale removal, which can only be improved by increasing the strip speed, which in turn makes scale removal less efficient because the resident time is decreased. This would have meant a local maximum in the profile of $\delta_{Cr_2O_3}$. However, for the parameter values used here, $\delta_{Cr_2O_3}$ decreases monotonically with $V^{(b)}$ for the two-phase model, as it did for the single-phase model.

Conclusions

In this paper, we have extended an earlier two-dimensional steady-state electrochemical model for the electrolytic pickling of stainless steel to include hydrodynamical two-phase effects which arise as a result of oxygen and hydrogen bubble generation from reacting surfaces. The new model predicts lower efficiency for the process than does the earlier single-phase model, principally because of bubble coverage of reacting surfaces. However, although the predicted gas-volume fraction at some reacting surfaces is almost as high as 0.5, the overall average current density at the steel strip surface under the two-phase flow assumption is perhaps no lower than 10% of its value when single-phase flow is assumed. The reason appears to be that although the blocking effect of the gas decreases the local current density, it also increases the local overpotential as compared to the situation when single-phase flow is assumed; overall, the local current density decreases only mildly.

Although the present model is already quite complex, still further additions are required, e.g., inclusion of turbulence, thermal effects, and extension to three dimensions. Other challenging tasks include the modeling of the downswing cycle of the vertical pickling process and the modeling of the horizontal pickling process.

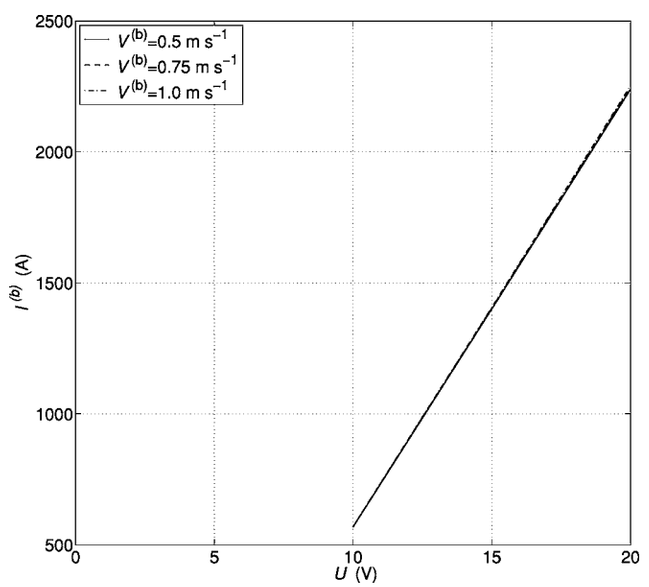

Figure 13. $I^{(b)}$ vs U for model 1, for three different strip speeds, $V^{(b)}$ (two-phase model).

Acknowledgments

Advice from Professor Fritz Bark, Dr. Anders Dahlkild, and Niklas Mellgren at the Department of Mechanics, Royal Institute of Technology, and the partial financial support of the Swedish Governmental Agency for Innovation Systems (VINNOVA) are gratefully acknowledged. The first author (N.I.) would also like to acknowledge the financial support of the Sweden-America Foundation and the Swedish Steel Producers Association, as well as the hospitality of Professor Noam Lior at the University of Pennsylvania.

Royal Institute of Technology assisted in meeting the publication costs of this article.

List of Symbols

a	gas bubble radius, m
a_i^{eq}	activity of ionic species i at atmospheric pressure, $i = H^+, OH^-$
a_j^{eq}	activity of nonionic species j at atmospheric pressure, $i = H_2, H_2O, O_2$
c_i	concentration of ionic species i, mol m^{-3}
c_j	concentration of nonionic species j, mol m^{-3}
$[D]$	characteristic ionic diffusion scale, m^2 s^{-1}
D_i	diffusion coefficient of ionic species i, m^2 s^{-1}
D_{eb}	electrode-to-strip distance, m
D_{ie}	interelectrode distance, m
$D_\parallel$	hydrodynamic self-diffusion constant
$D_\perp$	hydrodynamic self-diffusion constant

d half thickness of the steel strip, m
$E^{eq}_{H_2}$ equilibrium potential for the hydrogen reaction, V
$E^{eq}_{O_2}$ equilibrium potential for the oxygen reaction, V
E^{eq}_{0,H_2} standard potential for hydrogen evolution, V
E^{eq}_{0,O_2} standard potential for oxygen evolution, V
$\mathbf{e}_x$ unit vector in the x direction
$\mathbf{e}_y$ unit vector in the y direction
F Faraday constant, 96485 C mol^{-1}
$f(\gamma)$ hindered velocity function, $f(\gamma) = (1 - \gamma)^2$
g gravitational acceleration, m s^{-2}
$\mathbf{i}$ current density vector
$i^{(b)}$ local current density at the steel strip surface
$I^{(b)}$ average current density at the steel-strip surface
$i_{Cr_2O_3}$ current density due to Reaction 3, A m^{-2}
i_{H_2} current density due to Reaction 1, A m^{-2}
i_{O_2} current density due to Reaction 2, A m^{-2}
$i^{(b)}_{0,H_2}$ exchange current density for the hydrogen evolution reaction at the steel strip, A m^{-2}
$i^{(b)}_{0,O_2}$ exchange current density for the oxygen evolution reaction
$L^{(b)}$ length of the steel strip, m
$M_{Cr_2O_3}$ molar weight of chromium oxide, kg mol^{-1}
M_{H_2} molar weight of hydrogen, kg mol^{-1}
M_{O_2} molar weight of oxygen, kg mol^{-1}
$\mathbf{n}$ normal unit vector at a domain boundary
$\mathbf{N}_i$ molar flux density vector of ionic species i, mol m^{-3} s^{-1}
p pressure, kg m^{-1} s^{-2}
P modified pressure, kg m^{-1} s^{-2}
Pe Péclet number
R universal gas constant, 8.31 J mol s^{-1}
Re_{2a} bubble Reynolds number
R_i reaction rate for ionic species i, mol m^{-4} s^{-1}
T absolute temperature, K
$\mathbf{u}$ mass-averaged velocity of the gas–liquid mixture, m s^{-1}
u x component of the mass-averaged velocity $\mathbf{u}$, m s^{-1}
v y component of the mass-averaged velocity $\mathbf{u}$, m s^{-1}
U cell voltage, V
U_S Stokes terminal rise velocity, m s^{-1}
$V^{(b)}$ velocity of the steel strip, m s^{-1}
We_{2a} bubble Weber number
x horizontal coordinate, m
X dimensionless horizontal coordinate
y vertical coordinate, m
Y dimensionless vertical coordinate
z_i charge number of ionic species i
$\alpha^{(b)}_{H_2}$ transfer coefficient for the hydrogen evolution reaction at the steel strip
$\alpha^{(b)}_{O_2}$ transfer coefficient for the oxygen evolution reaction at the steel strip
$\alpha^{(c)}_{H_2}$ transfer coefficient for the hydrogen evolution reaction at the cathode electrode
$\alpha^{(a)}_{O_2}$ transfer coefficient for the oxygen evolution reaction at the anode electrode
β empirical function for shear-induced hydrodynamic diffusion
γ gas fraction of hydrogen and oxygen bubbles
γ_m volume fraction for maximum packing
η_{O_2} anodic surface overpotential, V
η_{H_2} cathodic surface overpotential, V
$\kappa^{(b)}$ electrical conductivity of the steel strip, S m^{-1}
Λ fraction of current at strip surface attributable to Reaction 3
$\Phi^{(b)}$ electric potential of the steel strip, V
$\Phi^{(e)}$ electric potential of the electrolyte, V
ρ_C density of the continuous phase, kg m^{-3}
$\rho_{Cr_2O_3}$ density of chromium oxide, kg m^{-3}
ρ_D density of the disperse phase, kg m^{-3}
ρ_{H_2} density of hydrogen, kg m^{-3}
ρ_{O_2} density of oxygen, kg m^{-3}
$\sigma_{Na_2SO_4}$ surface tension of aqueous sodium sulfate, N m^{-1}

Subscripts

C continuous phase
Cr_2O_3 chromium oxide
$Cr_2O_7^{2-}$ dichromate ion
D disperse phase
H^+ hydrogen ion
H_2 hydrogen bubble
H_2O water
i ionic species i
j nonionic species j
Na^+ sodium ion
Na_2SO_4 sodium sulfate
O_2 oxygen bubble
OH^- hydroxide ion
S Stokes terminal velocity
SO_4^{2-} sulfate ion

Superscripts

(a) anode
(b) steel strip
(c) cathode
(e) electrolyte
eq equilibrium value

References

1. L.-F. Li and J.-P. Celis, *Can. Metall. Q.*, **42**, 365 (2003).
2. E. T. Shapovalov, A. P. Shlyamnev, E. A. Ulyanin, V. D. Nikitin, A. R. Fisher, D. B. Goldzon, L. V. Popova, and I. I. Milovanov, *Steel in the USSR*, **12**, 215 (1982).
3. K. Tano, T. Murase, A. Maruta, S. Abe, T. Okazaki, and S. Kido, *Nippon Steel Technical Report*, **43** (1989).
4. D. Henriet, Final Report EUR 17248 EN, Technical report, Office for Official Publications of the European Communities, Luxembourg (1996).
5. W. Karner and J. Starcevic, U.S. Pat. 6,120,971 (2000).
6. E. Braun, *Iron Steel Eng.*, **57**, 79 (1980).
7. V. I. Dunaevskii, V. T. Stepanenko, M. A. Shnyl, and L. N. Bespalko, *Prot. Met.*, **21**, 359 (1985).
8. E. T. Shapovalov and A. P. Shlyamnev, in *International Conference on the 21st Century Steel Industry of Russia and CIS, Moscow*, Vol. V, pp. 59–60 (1994).
9. S. Kiya, Y. Hayashi, T. Kojima, and Y. Hyugaji, *Tetsu to Hagane*, **81**, 1007 (1985).
10. J. M. K. Hildén, J. V. A. Virtanen, and R. L. K. Ruoppa, *Mater. Corros.*, **51**, 728 (2000).
11. J. Hildén, J. Virtanen, O. Forsén, and J. Aromaa, *Electrochim. Acta*, **46**, 3859 (2001).
12. N. Ipek, N. Lior, F. H. Bark, A. Eklund, and A. Alemany, *Russ. J. Electrochem.*, **38**, 238 (2002).
13. N. Ipek, N. Lior, M. Vynnycky, and F. H. Bark, *J. Appl. Electrochem.*, **36**, 1367 (2006).
14. N. Ipek, A. Cornell, and M. Vynnycky, *J. Electrochem. Soc.*, **154**, P108 (2007).
15. B. Nussbaumer, Master's Thesis, Technischen Universität Wien, Austria (2001).
16. A. A. Dahlkild, *J. Fluid Mech.*, **428**, 249 (2001).
17. R. Wedin and A. A. Dahlkild, *Ind. Eng. Chem. Res.*, **40**, 5228 (2001).
18. M. D. Mat, K. Aldas, and O. J. Ilegbusi, *Int. J. Hydrogen Energy*, **29**, 1015 (2004).
19. K. Aldas, *Appl. Math. Comput.*, **154**, 507 (2004).
20. M. D. Mat and K. Aldas, *Int. J. Hydrogen Energy*, **30**, 411 (2005).
21. J. S. Newman and K. E. Thomas-Alyea, *Electrochemical Systems*, 3rd ed., John Wiley and Sons, New York (2004).
22. R. E. de la Rue and C. W. Tobias, *J. Electrochem. Soc.*, **106**, 827 (1959).
23. C. W. Tobias, *J. Electrochem. Soc.*, **106**, 833 (1959).
24. R. E. Meredith and C. W. Tobias, *J. Electrochem. Soc.*, **110**, 1257 (1963).
25. D. A. G. Bruggeman, *Ann. Phys.*, **24**, 636 (1935).
26. M. Ishii and N. Zuber, *AIChE J.*, **25**, 843 (1979).
27. H. Nicolai, B. Herzhaft, E. J. Hinch, L. Oger, and E. Guazzelli, *Phys. Fluids*, **7**, 12 (1995).
28. D. Leighton and A. Acrivos, *J. Fluid Mech.*, **181**, 415 (1987).
29. H. Vogt, *Electrochim. Acta*, **29**, 167 (1984).
30. L. J. J. Janssen, C. W. M. P. Sillen, E. Barendrecht, and S. J. D. van Stralen, *Electrochim. Acta*, **29**, 633 (1984).
31. *Comsol Multiphysics 3.3a*, http://www.comsol.com (2007).
32. W. J. Moore, *Basic Physical Chemistry*, 2nd ed., Prentice-Hall International Editions, London (1983).
33. D. R. Lide, *Handbook of Chemistry and Physics*, 84th ed., CRC Press, Boca Raton, FL (2003).